Supporting Information:

Plasma catalysis for ammonia synthesis:
A microkinetic modelling study on the contributions of Eley-Rideal reactions

Yannick Engelmann*[a], Kevin van 't Veer[a,b], Yury Gorbanev[a], Erik Cornelis Neyts[a], William F. Schneider[c], Annemie Bogaerts[a]

* Corresponding author email: yannick.engelmann@uantwerpen.be
[a] Department of Chemistry, Research Group PLASMANT, PLASMA and NANOLab Centers of Excellence,
Universiteit Antwerpen, Universiteitsplein 1, 2610 Wilrijk-Antwerp, Belgium
[b] Université Libre de Bruxelles, Faculty of Sciences, Chemistry of Surfaces, Interfaces and Nanomaterials,
CP255, Avenue F. D. Roosevelt 50, B-1050 Brussels, Belgium
[c] Department of Chemical and Biomolecular Engineering, University of Notre Dame,
Notre Dame, IN, 46556, USA

Number of pages: S1-S20
Number of figures: 12
Number of tables: 6

1. Kinetic data

To construct the activation barrier, $\Delta H^{\ddagger}$, of the forward and backward reactions in column 1 of Table 1 in the main article, we made use of the scaling relations previously reported by Mehta *et al.*[1] The scaling relations are linear correlations between the N* binding energy, E_b, and the activation barrier and reaction energy, computed via DFT using the RPBE functional.[2]

$$\Delta H_r = \gamma_r E_b + \xi_r$$

$$\Delta H^{\ddagger} = \gamma_a E_b + \xi_a$$

The parameters of the fit, γ and ξ, are tabulated in Table S1 and explained in more detail in [1].

Table S1: Parameters of the linear scaling relations between the N* binding energy and the reaction energy and activation barrier.

Reactions	**Reaction energy**		**Activation barrier**	
	γ_r	ξ_r	γ_a	ξ_a
$H_2 + 2^* \rightleftharpoons 2H^*$	0.00	-0.64	0.00	0.00
$N_2 + 2^* \rightleftharpoons 2H^*$	2.00	0.00	1.56	2.32
$N^* + H^* \rightleftharpoons NH^*$	-0.56	-0.20	-0.28	1.71
$NH^* + H^* \rightleftharpoons NH_2^*$	-0.43	0.10	-0.09	1.24
$NH_2^* + H^* \rightleftharpoons NH_3$	-0.45	0.21	-0.38	1.03

The enthalpy barriers of the radical adsorption reactions in column 2 of Table 1 in the main article are assumed zero. The enthalpy barriers of the ER reactions in column 3 and 4 of Table 1 are assumed zero for the calculations in *1.3. Impact of Eley-Rideal reactions.* In section *1.4 Sensitivity analysis of the Eley-Rideal barriers,* the barriers of the reactions in column 3 and 4 are varied from 0 eV to 5 eV, for each column separately, while keeping the barriers of the other column zero.

Table S2 lists the reaction entropies and entropy barriers for all of the reactions included in the model. The entropies of the gas phase species are calculated with the formula[3]:

$$S(T) = S^{\circ}_{298K} - S_{trans}(298K) + S_{trans}(T)$$

Where the standard gas phase entropy, S°(298K), can be found in the database of the National Institute of Standards and Technology (https://webbook.nist.gov/chemistry/), and $S_{trans}(T)$ is the translational part of the entropy at temperature T:[3,4]

$$S_{trans}(T) = R\ln\left(\frac{k_B T}{p}\frac{(2\pi m k_B T)^{3/2}}{h^3}e^{5/2}\right)$$

The entropy of surface species and transition states were assumed to be zero.

Table S2: Reaction entropies and entropy barriers of all the reactions in the model

Reactions	**ΔS_r**	**$\Delta S^{‡}$**
$H_2 + 2^* \rightleftharpoons 2H^*$	$-S_{H2}$	$-S_{H2}$
$N_2 + 2^* \rightleftharpoons 2H^*$	$-S_{N2}$	$-S_{N2}$
$N^* + H^* \rightleftharpoons NH^*$	0.00	0.00
$NH^* + H^* \rightleftharpoons NH_2^*$	0.00	0.00
$NH_2^* + H^* \rightleftharpoons NH_3$	S_{NH3}	S_{NH3}
$H + ^* \rightleftharpoons H^*$	$-S_H$	$-S_H$
$N + ^* \rightleftharpoons N^*$	$-S_N$	$-S_N$
$NH + ^* \rightleftharpoons NH^*$	$-S_{NH}$	$-S_{NH}$
$NH_2 + ^* \rightleftharpoons NH_2^*$	$-S_{NH2}$	$-S_{NH2}$
$H + H^* \rightleftharpoons H_2$	$S_{H2} - S_H$	$-S_H$
$N + H^* \rightleftharpoons NH^*$	$-S_N$	$-S_N$
$NH + H^* \rightleftharpoons NH_2^*$	$-S_{NH}$	$-S_{NH}$
$NH_2 + H^* \rightleftharpoons NH_3$	$S_{NH3} - S_{NH2}$	$-S_{NH2}$
$H + N^* \rightleftharpoons NH^*$	$-S_H$	$-S_H$
$H + NH^* \rightleftharpoons NH_2^*$	$-S_H$	$-S_H$
$H + NH_2^* \rightleftharpoons NH_3$	$-S_H$	$-S_H$
$N + N^* \rightleftharpoons N_2$	$S_{N2} - S_N$	$-S_N$

2. Radical densities

Table S3 tabulates the radical densities used in our microkinetic models, as obtained from a plasma chemical kinetics model, using ZDPlasKin, reported by van ‘t Veer *et al.*[5]

Table S3: Densities of plasma species (m^{-3}) in the micro-discharges and the afterglows of a filamentary DBD and in a uniform discharge, obtained with ZDPlasKin.

Species	Filam. micro-discharge	Filam. afterglow	Uniform
$N_{2(g)}$	1.37×10^{25}	1.38×10^{25}	9.70×10^{24}
$H_{2(g)}$	4.53×10^{24}	4.53×10^{24}	4.27×10^{24}
N	4.49×10^{20}	1.10×10^{18}	2.72×10^{21}
H	1.82×10^{21}	3.29×10^{19}	2.15×10^{23}
NH	1.80×10^{17}	1.12×10^{16}	7.30×10^{18}
NH_2	1.53×10^{14}	1.92×10^{17}	8.90×10^{18}
NH_3	4.96×10^{15}	2.98×10^{20}	5.89×10^{21}

Table S4: Populations of the levels of vibrational excitation of N_2, thermal Boltzmann at 400 K, in the microdischarges and the afterglows of a filamentary plasma (ZDPlasKin), in a uniform plasma (ZDPlasKin), and for a Treanor distribution at 3000 K.

Level (eV)	**Boltzmann**	**Microdischarge**	**Afterglow**	**Uniform**	**Treanor**
0.00	1.00E+00	9.95E-01	9.98E-01	7.06E-01	6.30E-01
0.29	2.31E-04	3.65E-03	2.36E-03	1.97E-01	2.14E-01
0.57	5.91E-08	6.52E-04	7.72E-06	6.17E-02	8.09E-02
0.86	1.68E-11	3.54E-04	1.53E-07	2.13E-02	3.42E-02
1.13	5.28E-15	1.76E-04	1.12E-08	8.02E-03	1.61E-02
1.41	1.84E-18	7.59E-05	7.22E-10	3.23E-03	8.48E-03
1.68	7.14E-22	2.86E-05	3.28E-11	1.37E-03	4.98E-03
1.95	3.07E-25	9.87E-06	1.06E-12	5.99E-04	3.27E-03
2.21	1.46E-28	3.19E-06	3.82E-14	2.64E-04	2.39E-03
2.47	7.73E-32	9.77E-07	2.31E-15	1.15E-04	1.96E-03
2.73	4.53E-35	2.82E-07	1.75E-16	4.92E-05	1.79E-03
2.98	2.95E-38	7.78E-08	1.30E-17	2.15E-05	1.82E-03
3.23	2.14E-41	2.12E-08	8.28E-19	9.70E-06	0.00E+00
3.48	1.72E-44	5.88E-09	4.12E-20	4.48E-06	0.00E+00
3.72	1.54E-47	1.74E-09	1.91E-21	2.10E-06	0.00E+00
3.96	1.53E-50	5.91E-10	1.14E-22	9.87E-07	0.00E+00
4.19	1.68E-53	2.38E-10	8.43E-24	4.58E-07	0.00E+00
4.42	2.07E-56	1.11E-10	5.61E-25	2.02E-07	0.00E+00
4.65	2.83E-59	5.32E-11	4.51E-26	8.13E-08	0.00E+00
4.87	4.31E-62	2.60E-11	5.18E-27	2.85E-08	0.00E+00
5.09	7.30E-65	1.48E-11	3.91E-28	8.57E-09	0.00E+00
5.31	1.38E-67	1.03E-11	2.67E-29	2.46E-09	0.00E+00
5.52	2.91E-70	6.57E-12	1.78E-30	8.68E-10	0.00E+00
5.73	6.83E-73	3.18E-12	1.27E-31	3.93E-10	0.00E+00
5.94	1.79E-75	1.98E-12	1.40E-32	2.07E-10	0.00E+00

3. Density Functional Theory (DFT) calculations

We performed DFT calculations using the VASP software to estimate the barriers of ER reactions on transition metal catalysts. Exchange-correlation effects are calculated with the Perdew-Burke-Ernzerhof (PBE) functional within the generalized gradient approximation (GGA). We used an energy cutoff of 440 eV to truncate the basis set, which is a typical value for these systems.[6,7]

Firstly, we optimized the bulk structures of each metal separately. Subsequently, we added adsorbates with specific distances to the surface, and calculated the energy on a 4x4x4 metal slab while keeping all coordinates (metal and adsorbates) fixed. This way we can obtain an upper limit to the activation barrier for ER reactions. The vacuum length was 14 Å, the Brillouin zone was sampled using the Monkhorst−Pack scheme with 4x4x1 k-points, the lattice constants for Ru, Ni and Cu were 3.81, 3.50 Å and 3.60 Å, respectively. All calculations were performed spin-polarized (ISPIN = 2). We used a smearing method (ISMEAR = 1) with a width of smearing equal to 0.1 eV (ISIGMA = 0.1). For more accurate calculations of binding energies, we suggest accounting for spin contamination errors.[7]

All calculations are performed in the absence of an electric field. As discussed by Rouwenhorst *et al.*[8], the effect of an electric field, induced by the plasma, on the binding energy of adsorbates is expected to be small. Both DFT calculations and experiments have shown that reduced electric fields, typical for DBDs, are too weak to have a significant impact on the reaction energies and barriers.

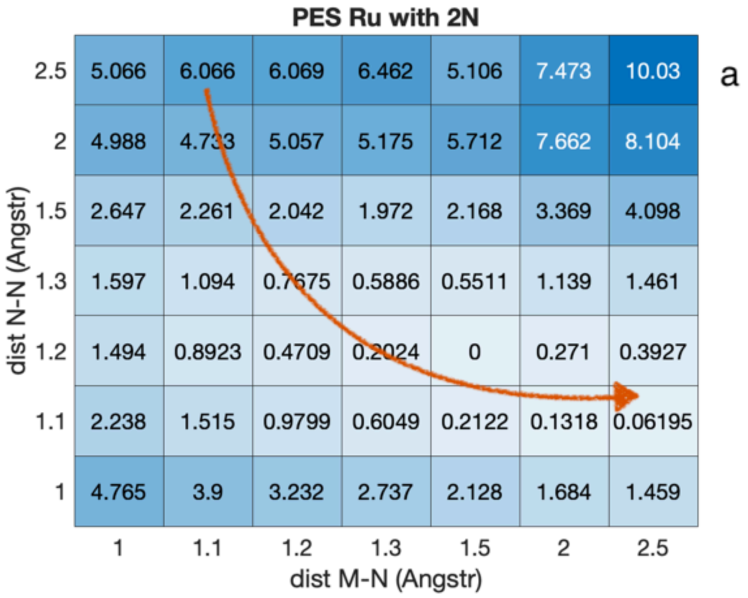
PES Ru with 2N

	1	1.1	1.2	1.3	1.5	2	2.5
2.5	5.066	6.066	6.069	6.462	5.106	7.473	10.03
2	4.988	4.733	5.057	5.175	5.712	7.662	8.104
1.5	2.647	2.261	2.042	1.972	2.168	3.369	4.098
1.3	1.597	1.094	0.7675	0.5886	0.5511	1.139	1.461
1.2	1.494	0.8923	0.4709	0.2024	0	0.271	0.3927
1.1	2.238	1.515	0.9799	0.6049	0.2122	0.1318	0.06195
1	4.765	3.9	3.232	2.737	2.128	1.684	1.459

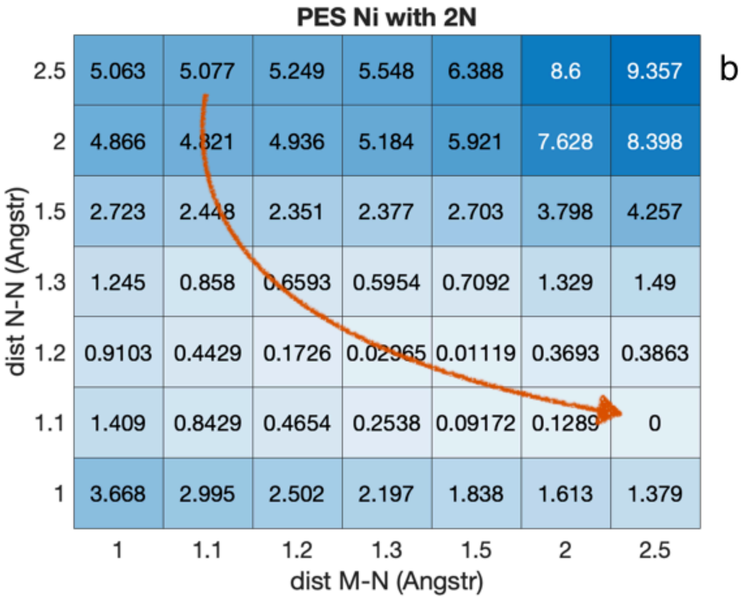
PES Ni with 2N

	1	1.1	1.2	1.3	1.5	2	2.5
2.5	5.063	5.077	5.249	5.548	6.388	8.6	9.357
2	4.866	4.821	4.936	5.184	5.921	7.628	8.398
1.5	2.723	2.448	2.351	2.377	2.703	3.798	4.257
1.3	1.245	0.858	0.6593	0.5954	0.7092	1.329	1.49
1.2	0.9103	0.4429	0.1726	0.02965	0.01119	0.3693	0.3863
1.1	1.409	0.8429	0.4654	0.2538	0.09172	0.1289	0
1	3.668	2.995	2.502	2.197	1.838	1.613	1.379

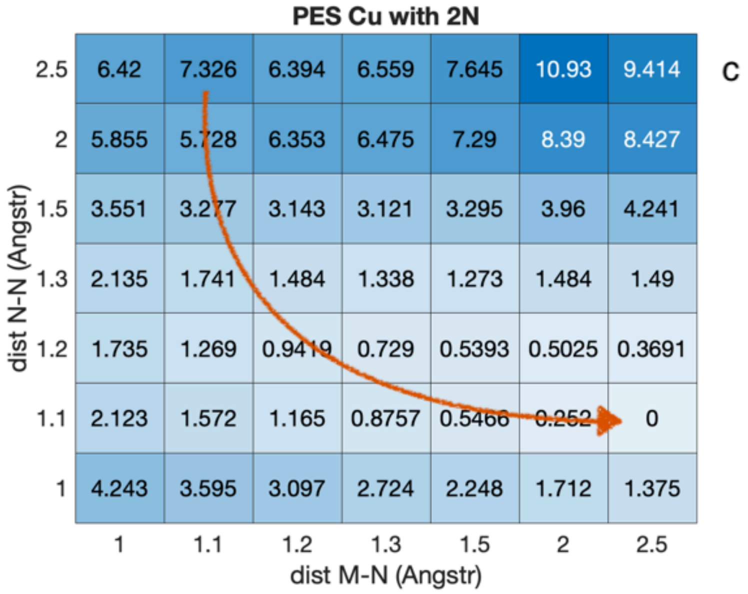
PES Cu with 2N

	1	1.1	1.2	1.3	1.5	2	2.5
2.5	6.42	7.326	6.394	6.559	7.645	10.93	9.414
2	5.855	5.728	6.353	6.475	7.29	8.39	8.427
1.5	3.551	3.277	3.143	3.121	3.295	3.96	4.241
1.3	2.135	1.741	1.484	1.338	1.273	1.484	1.49
1.2	1.735	1.269	0.9419	0.729	0.5393	0.5025	0.3691
1.1	2.123	1.572	1.165	0.8757	0.5466	0.252	0
1	4.243	3.595	3.097	2.724	2.248	1.712	1.375

Figure S1: DFT calculated potential energy surfaces (PES) of the N + N* → $N_{2(g)}$ ER reaction on three catalysts, i.e., Ru, Ni, and Cu, representing a non-noble, intermediate and noble catalyst, respectively.
The energies are shown with respect to the most stable configuration.

The results on the ER reaction N + N* → $N_{2(g)}$ on Ru, Ni and Cu are shown in Figure S1. The lightest cell indicates the most stable configuration and the arrow indicates the minimum energy path of the reaction. For Cu and Ni, the most stable configuration (lightest cell) is N_2 in the gas phase (long metal-N distance, and short N-N distance). On Ru the most stable configuration is a physisorbed state of molecular N_2 at a distance of 1.5 Å from the surface.

The initial state of the ER reaction is one N atom at the surface (short metal-N distance of 1.1 Å) and one N atom in the gas phase (long N-N distance of 2.5 Å). The final state of the ER reaction is an N_2 molecule in the gas phase (long M-N distance of 2.5 Å, and short N-N distance of 1.1 Å). Figure S1 suggests, as indicated by the arrow, that for the three cases (non-noble (Ru), intermediate (Ni) and noble (Cu) catalyst), the system can move without barrier from the initial state down to the desorbed N_2(g) state.

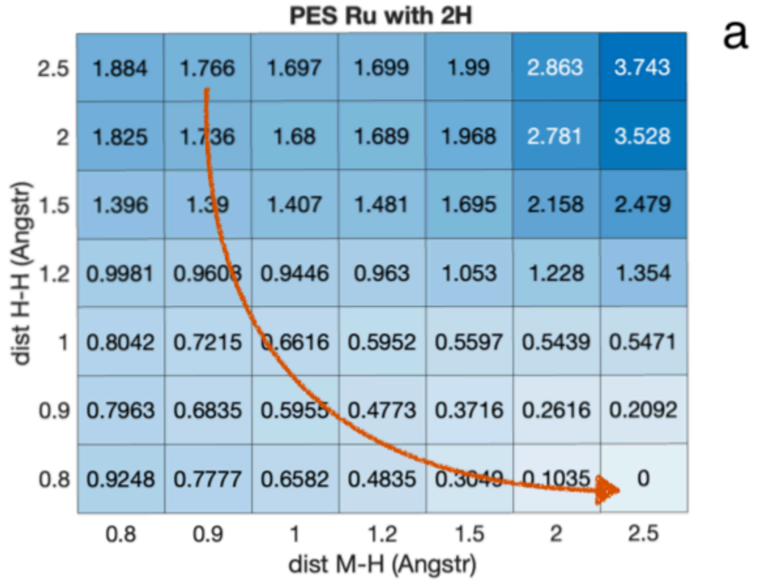

a

PES Ru with 2H

dist H-H (Angstr) \ dist M-H (Angstr)	0.8	0.9	1	1.2	1.5	2	2.5
2.5	1.884	1.766	1.697	1.699	1.99	2.863	3.743
2	1.825	1.736	1.68	1.689	1.968	2.781	3.528
1.5	1.396	1.39	1.407	1.481	1.695	2.158	2.479
1.2	0.9981	0.9608	0.9446	0.963	1.053	1.228	1.354
1	0.8042	0.7215	0.6616	0.5952	0.5597	0.5439	0.5471
0.9	0.7963	0.6835	0.5955	0.4773	0.3716	0.2616	0.2092
0.8	0.9248	0.7777	0.6582	0.4835	0.3049	0.1035	0

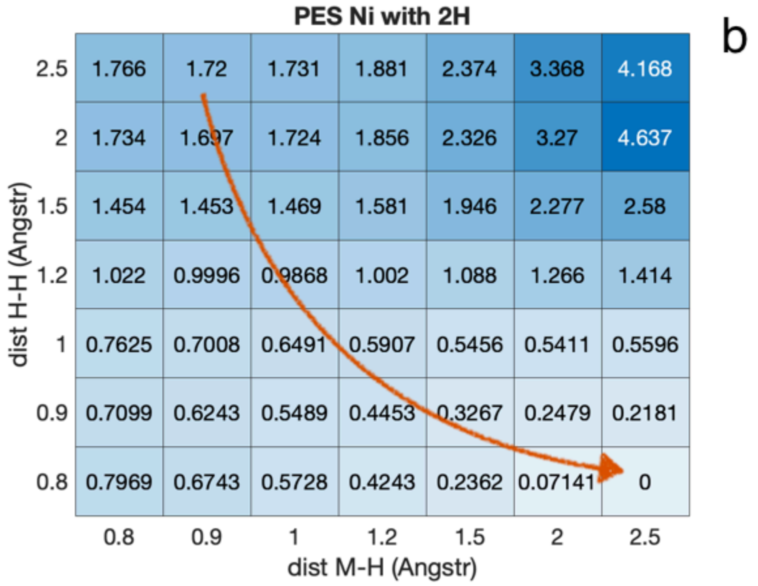

b

PES Ni with 2H

dist H-H (Angstr) \ dist M-H (Angstr)	0.8	0.9	1	1.2	1.5	2	2.5
2.5	1.766	1.72	1.731	1.881	2.374	3.368	4.168
2	1.734	1.697	1.724	1.856	2.326	3.27	4.637
1.5	1.454	1.453	1.469	1.581	1.946	2.277	2.58
1.2	1.022	0.9996	0.9868	1.002	1.088	1.266	1.414
1	0.7625	0.7008	0.6491	0.5907	0.5456	0.5411	0.5596
0.9	0.7099	0.6243	0.5489	0.4453	0.3267	0.2479	0.2181
0.8	0.7969	0.6743	0.5728	0.4243	0.2362	0.07141	0

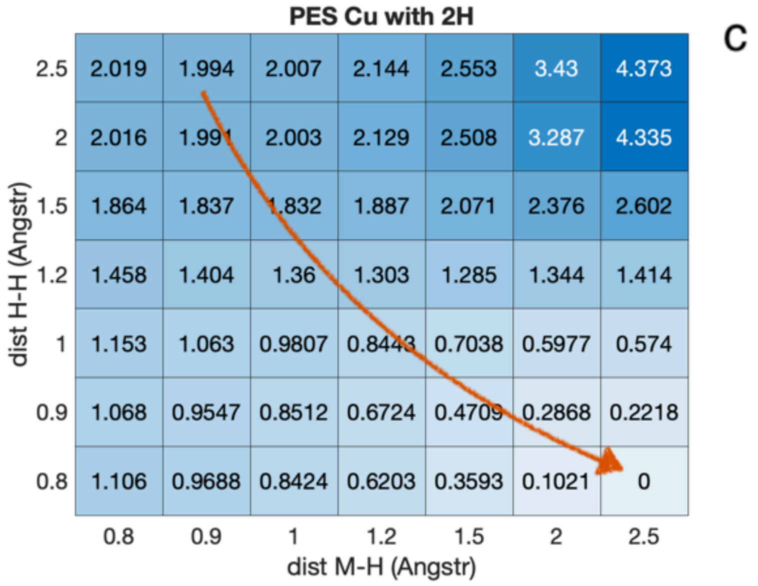

c

PES Cu with 2H

dist H-H (Angstr) \ dist M-H (Angstr)	0.8	0.9	1	1.2	1.5	2	2.5
2.5	2.019	1.994	2.007	2.144	2.553	3.43	4.373
2	2.016	1.991	2.003	2.129	2.508	3.287	4.335
1.5	1.864	1.837	1.832	1.887	2.071	2.376	2.602
1.2	1.458	1.404	1.36	1.303	1.285	1.344	1.414
1	1.153	1.063	0.9807	0.8443	0.7038	0.5977	0.574
0.9	1.068	0.9547	0.8512	0.6724	0.4709	0.2868	0.2218
0.8	1.106	0.9688	0.8424	0.6203	0.3593	0.1021	0

Figure S2: DFT calculated potential energy surfaces (PES) of the H + H* → $H_{2(g)}$ ER reaction on three catalysts, i.e., Ru, Ni, and Cu, representing a non-noble, intermediate and noble catalyst, respectively.
The energies are shown with respect to the most stable configuration.

The results on the ER reaction H + H* → $H_{2(g)}$ on Ru, Ni and Cu are presented in Figure S2. The initial state of the ER reaction is one H atom at the surface (short metal-H distance of 0.9 Å) and one N atom in the gas phase (long H-H distance of 2.5 Å). The final state of the ER reaction, is a H_2 molecule in the gas phase (long M-H distance of 2.5 Å, and short N-N distance of 0.8 Å). Figure S2 suggests, as indicated by the arrow, that for the three cases (non-noble (Ru), intermediate (Ni) and noble (Cu) catalyst), the system can move without barrier from the initial state down to the desorbed H_2(g) state.

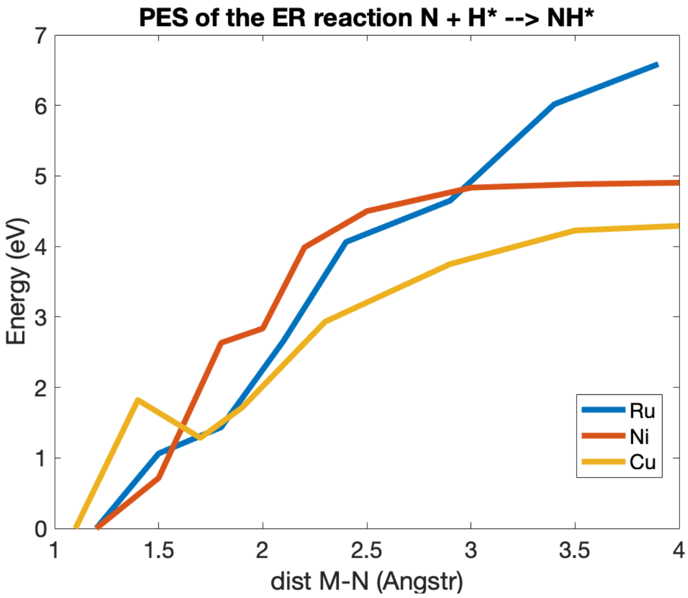

Figure S3: DFT calculated potential energy surfaces (PES) of the N + H* → NH* ER reaction on three catalysts, i.e., Ru, Ni, and Cu, representing a non-noble, intermediate and noble catalyst, respectively.
The energies are shown with respect to the most stable configuration.

Finally, Figure S3 illustrates the results for the ER reaction N + H* → NH* on Ru, Ni and Cu. The initial state of the ER reaction is one H atom at the surface and one N atom in the gas phase (long H-H distance of 4 Å). The final state of the ER reaction, is an NH* radical adsorbed to the metal (attached via the N atom). Figure S3 suggests, that for the three cases (non-noble

(Ru), intermediate (Ni) and noble (Cu) catalyst), the system can move without barrier from the initial state down to the adsorbed NH* state.

4. Sensitivity analysis of the ER barriers in the afterglows of a filamentary plasma

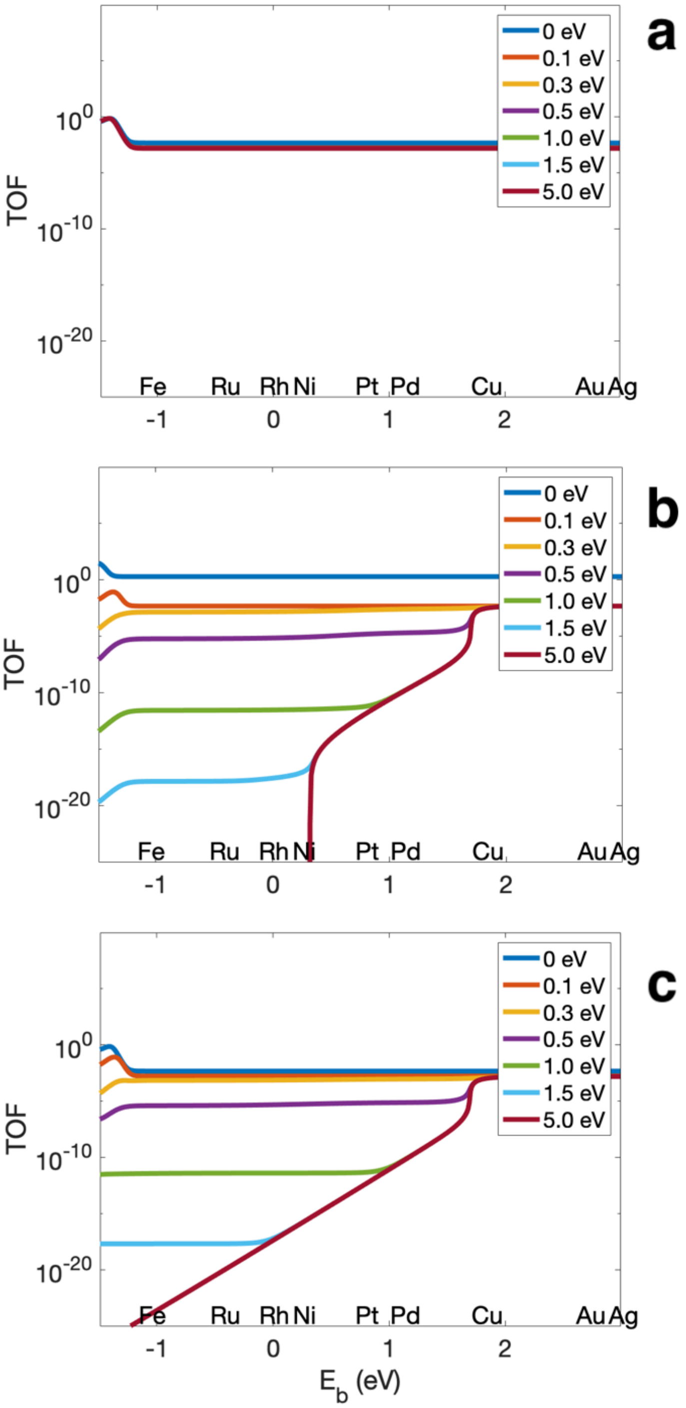

Figure S4: Calculated NH_3 TOF in the afterglows of a filamentary plasma for different barriers of the ER reactions in Table 1 (a) column 3, (b) column 4 and (c) columns 3 and 4 together.

5. Sensitivity analysis of the ER barriers in the uniform plasma

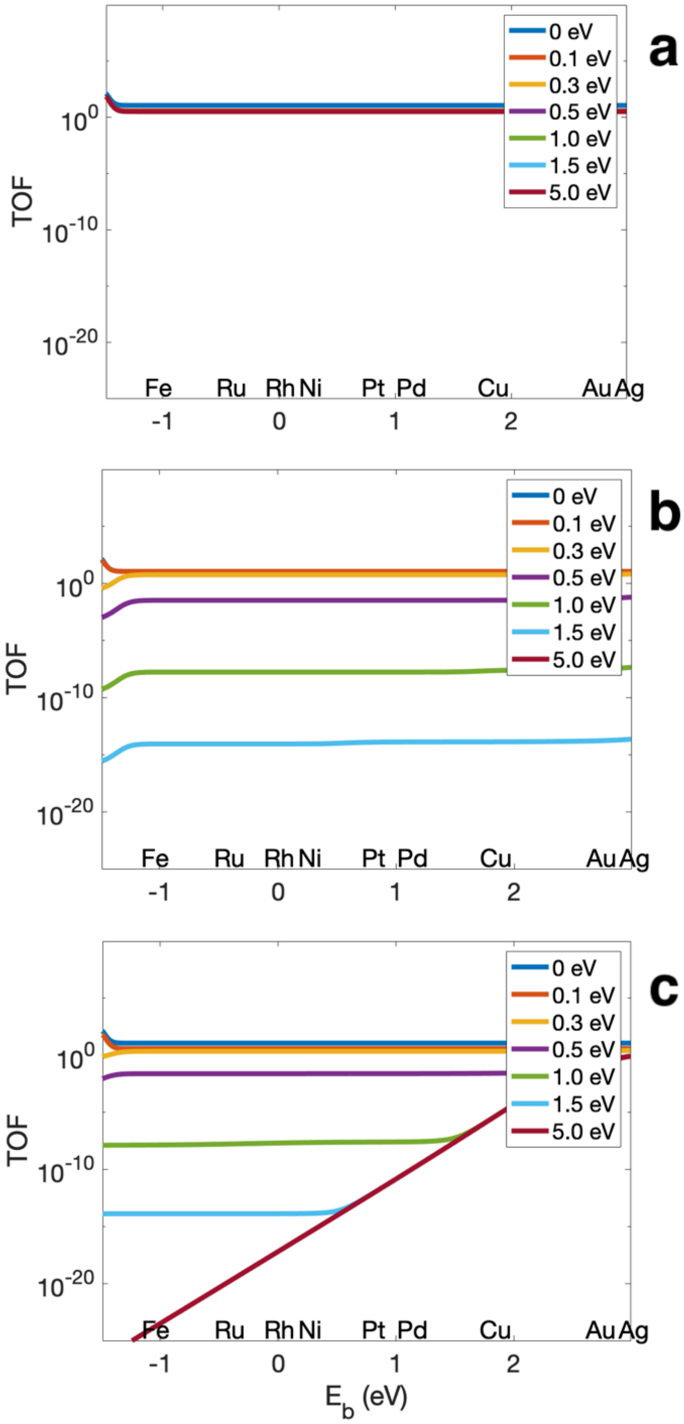

Figure S5: Calculated NH_3 TOF in the uniform plasma for different barriers of the ER reactions in Table 1 (a) column 3, (b) column 4, and (c) columns 3 and 4 together.

6. Reaction rates in a filamentary plasma

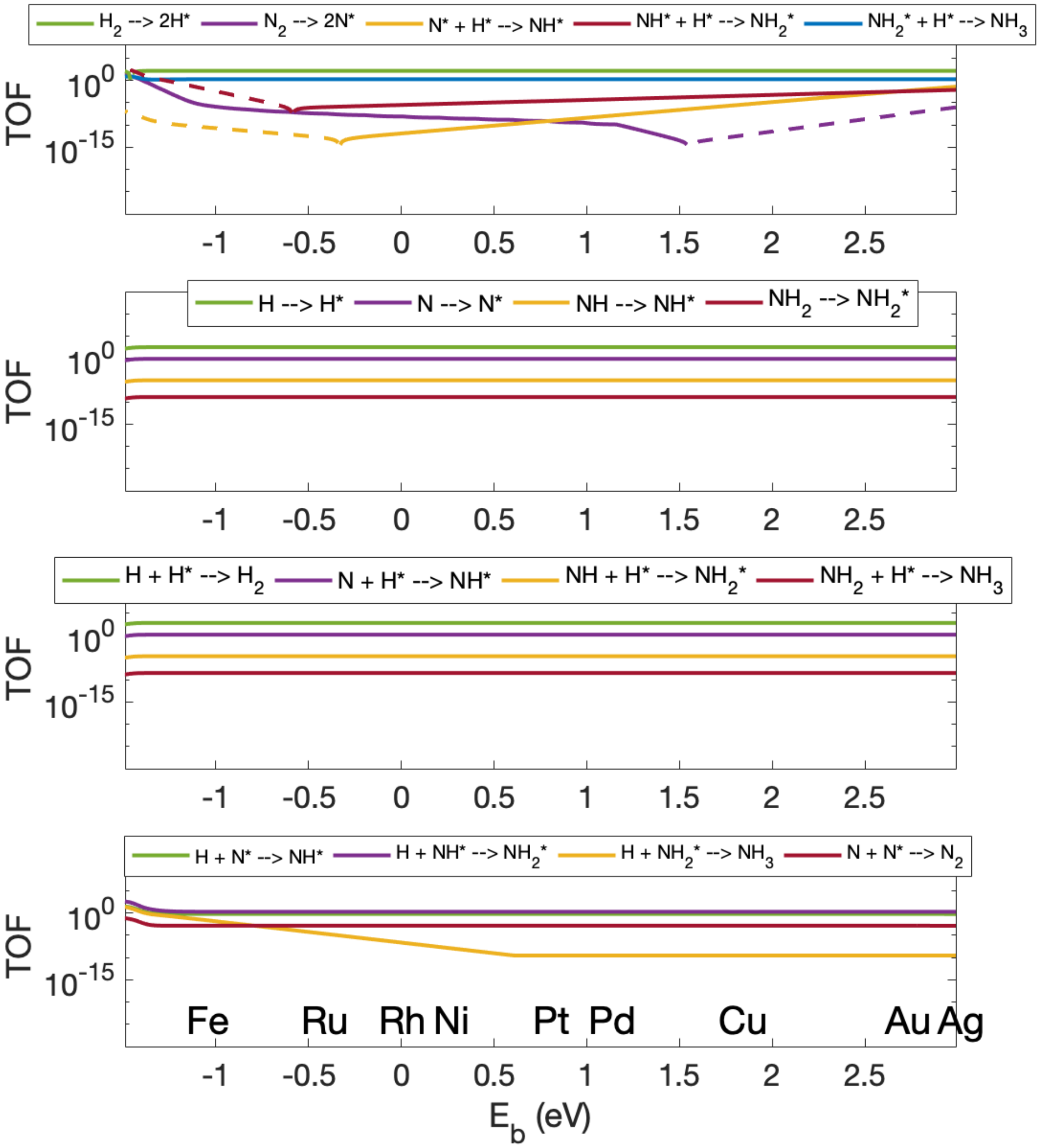

Figure S6: Steady state reaction rates of the plasma-catalytic NH$_3$ synthesis during a micro-discharge of a filamentary plasma, as a function of N* binding energy.

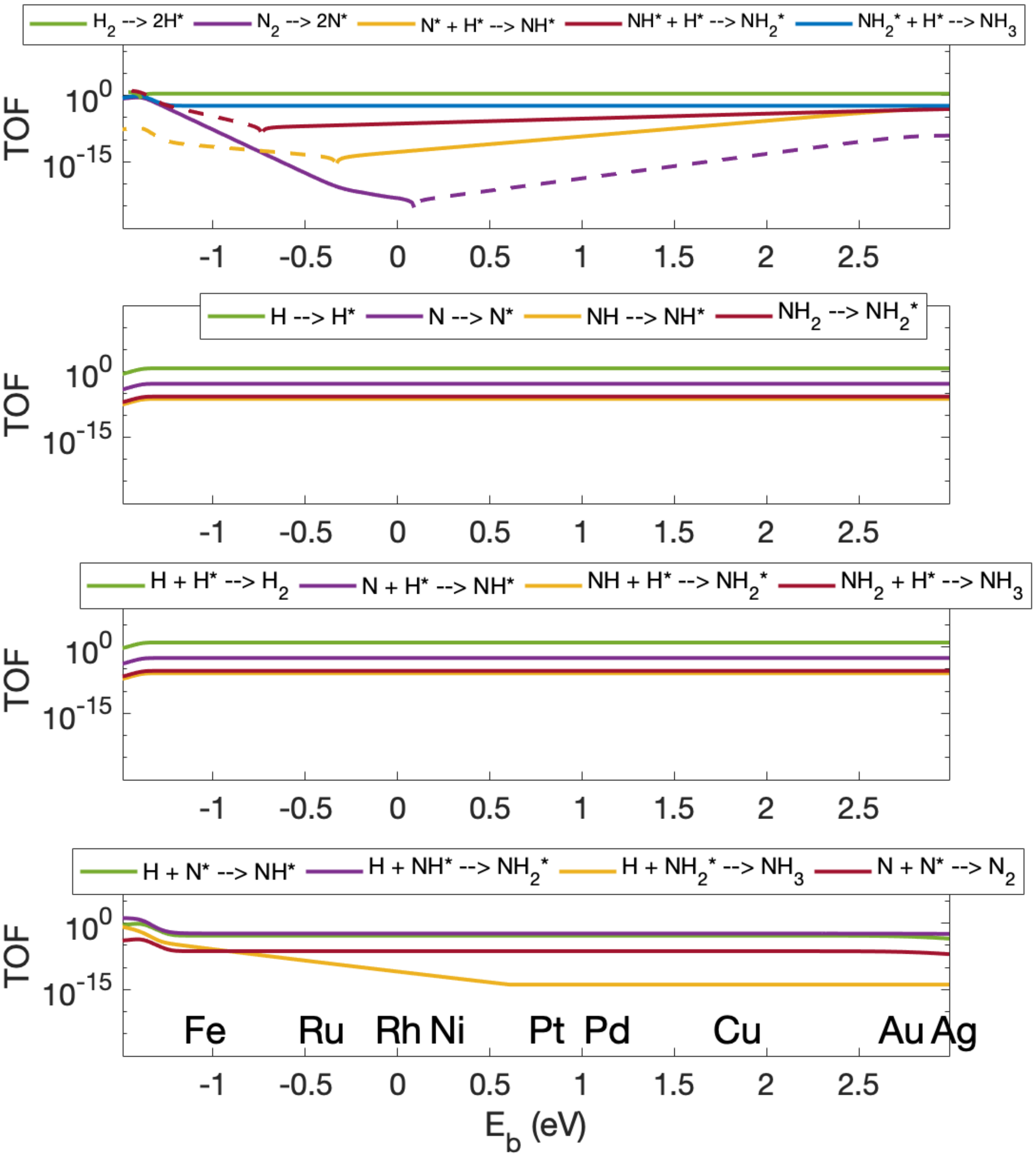

Figure S7: Steady state reaction rates of the plasma-catalytic NH_3 synthesis during the afterglows of a filamentary plasma, as a function of the N* binding energy.

7. Reaction pathways in the afterglows of the filamentary discharge

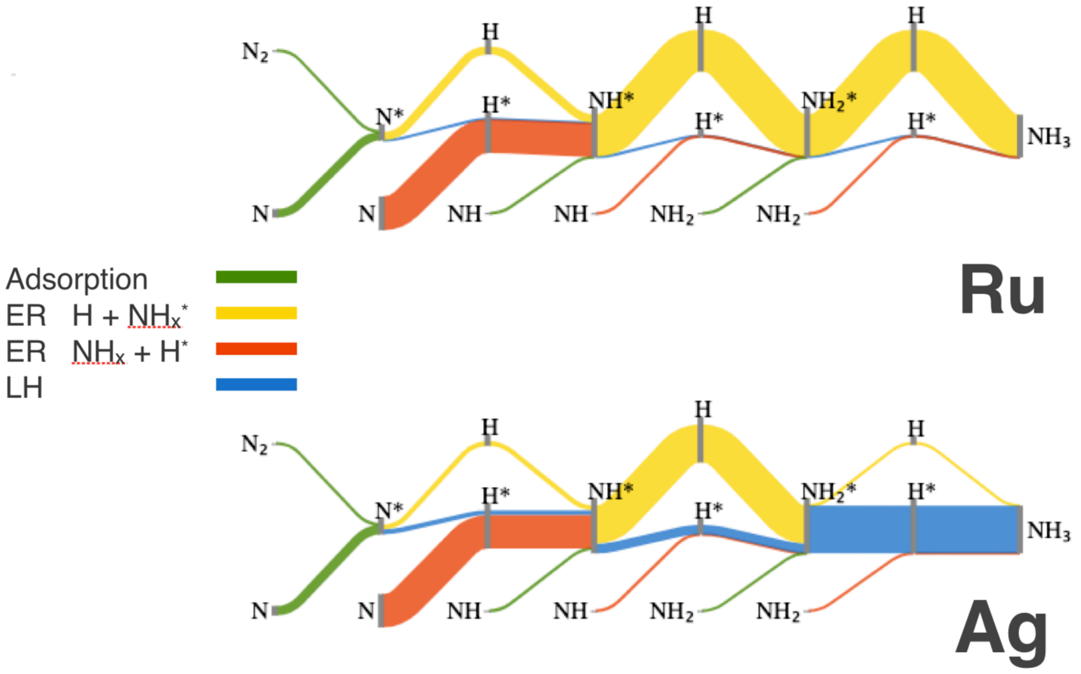

Figure S8: Reaction flow diagrams for plasma-catalytic NH_3 synthesis on a non-noble catalyst (Ru) and a noble catalyst (Ag), presenting the relative weight of the various reaction rates, in a filamentary DBD, in the afterglow of the filaments.

8. TOFs at 700K

In Figure S9 we show the calculated TOFs corresponding to the input data from plasma chemistry modelling for a gas phase ratio of 3:1 N_2/H_2 at 700K in the filamentary plasma. When radicals are added to the gas phase, the NH_3 TOF is still significantly increased compared to when only vibrational excitations are included.

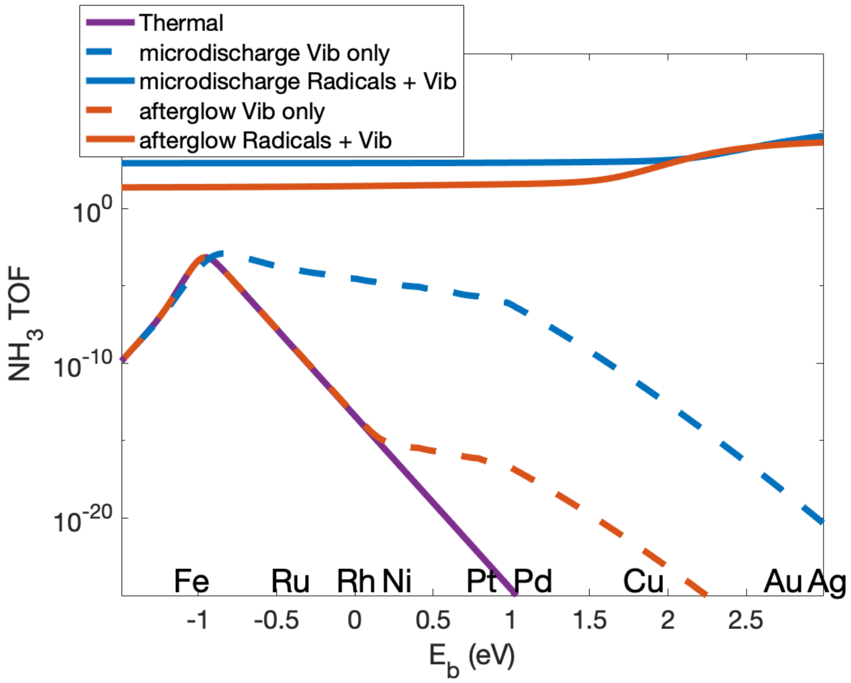

Figure S9: Calculated NH_3 TOF in the micro-discharges (blue) and afterglows (red) of a filamentary plasma at 700 K. The full lines represent plasmas including both radicals and vibrational excitations, the dashed lines represent plasmas including only vibrational excitation, without radicals.

In Figure S10 we depict the reaction rates of each of the individual elementary reactions in the micro-discharges of the filamentary plasma (corresponding to the full blue line in Fig. S9). The blue line from Fig. S9 overlaps with the LH reactions in the top graph of Fig S10 (yellow, red and blue lines, representing N* + H*, NH* + H* and NH_2* + H*, respectively). Due to the increased activity of the catalysts at higher temperature the LH reactions are now more important than the ER reactions.

However, the N source in NH_3 is still the adsorption of N atoms, rather than the catalytic dissociation of N_2, explaining why radical TOFs are still higher than the TOFs from vibrational excitation (cf. Fig S9).

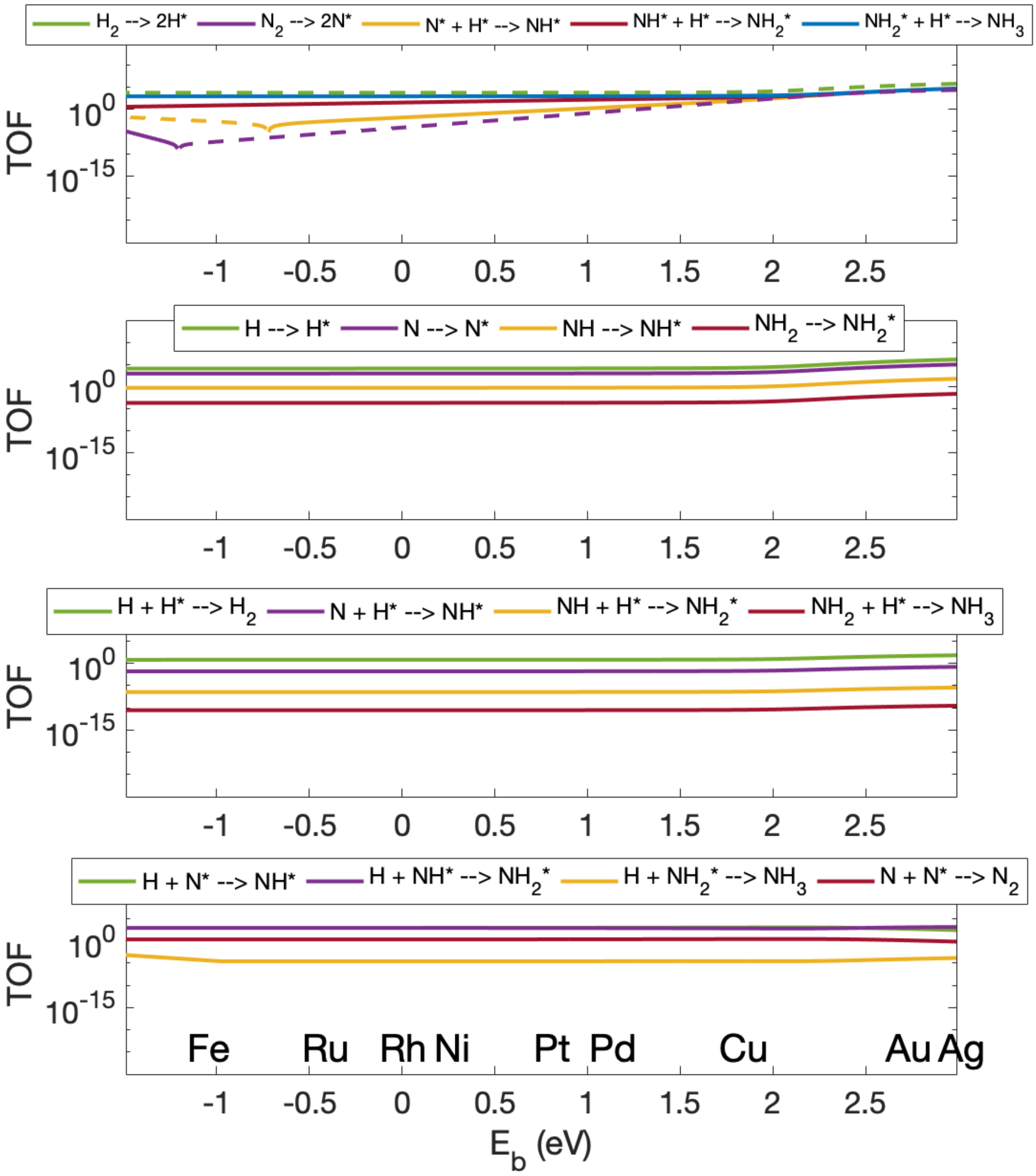

Figure S10: Steady state reaction rates of the plasma-catalytic NH_3 synthesis during the afterglows of a filamentary plasma, as a function of the N* binding energy.

9. Ratio of contribution of ER to LH reactions

Table S5: Ratio of the contributions of ER to LH reactions of the microdischarges of the filamentary plasma. (To be compared with Figure 6 of the main article)

	Rate (s^{-1})	**Rate (s^{-1})**	**Rate (s^{-1})**	**Ratios**
	N* + H*	**N + H***	**H + N***	**ER/LH**
Ru	3.00×10^{-13}	1.33	5.90×10^{-1}	6.39×10^{12}
Ag	7.10×10^{-3}	1.33	5.90×10^{-1}	2.70×10^{2}
	NH* + H*	**NH + H***	**H + NH***	
Ru	7.28×10^{-7}	1.87×10^{-5}	1.92	2.63×10^{6}
Ag	7.10×10^{-3}	1.87×10^{-5}	1.92	2.70×10^{2}
	NH_2* +H*	**NH_2 +H***	**H + NH_2***	
Ru	2.05×10^{-6}	1.00×10^{-6}	1.92	9.35×10^{5}
Ag	1.92	1.00×10^{-6}	2.92×10^{-10}	5.22×10^{-7}

10. Coverage of species in the afterglows of the filamentary plasma

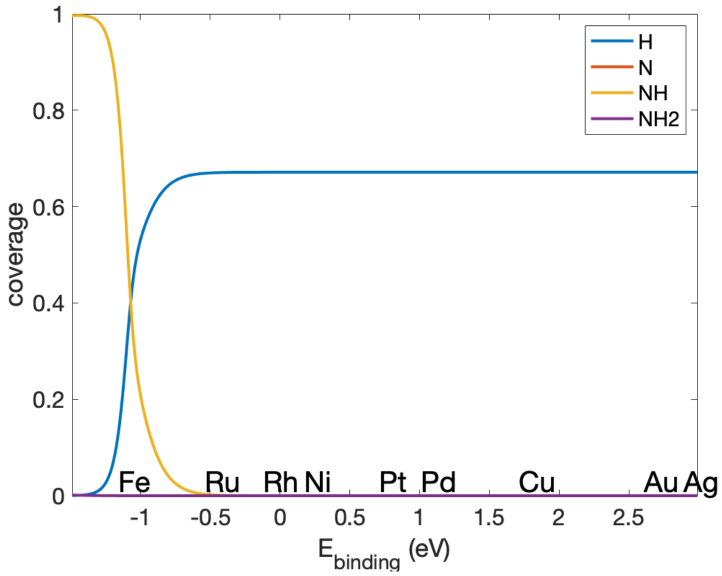

Figure S11: Steady state catalyst coverage as function of the binding energy during the afterglows of the filamentary plasma

11. Simulation of different gas ratios

In Fig S12 we show the impact of different gas ratios on the NH_3 TOFs in the micro-discharges of the filamentary plasma.

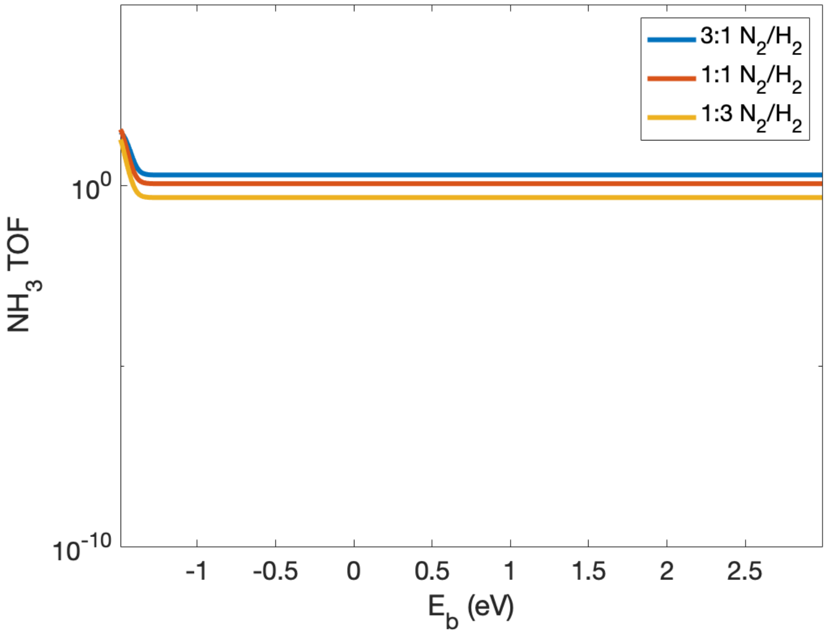

Figure S12: Calculated NH_3 TOF in the micro-discharges of a filamentary plasma for different gas phase ratios.

Table S6: Densities of plasma species (m^{-3}) in the micro-discharges and the afterglows of a filamentary DBD and in a uniform discharge, obtained with ZDPlasKin.

Species	**3:1**	**1:1**	**1:3**
$N_{2(g)}$	1.37 x10^{25}	9.17 x10^{24}	4.59 x10^{24}
$H_{2(g)}$	4.53 x10^{24}	9.13 x10^{24}	1.37 x10^{25}
N	4.49 x10^{20}	2.56 x10^{20}	1.06 x10^{20}
H	1.82 x10^{21}	3.98 x10^{21}	6.33 x10^{21}
NH	1.80 x10^{17}	2.19 x10^{17}	1.40 x10^{17}
NH_2	1.53 x10^{14}	1.17 x10^{14}	7.53 x10^{13}
NH_3	4.96 x10^{15}	1.47 x10^{15}	1.95 x10^{15}

References

(1) Mehta, P.; Barboun, P.; Herrera, F. A.; Kim, J.; Rumbach, P.; Go, D. B.; Hicks, J. C.; Schneider, W. F. Overcoming Ammonia Synthesis Scaling Relations with Plasma-Enabled Catalysis. *Nat. Catal.* **2018**, *1* (4), 269–275. https://doi.org/10.1038/s41929-018-0045-1.

(2) Hummelshøj, J. S.; Abild-Pedersen, F.; Studt, F.; Bligaard, T.; Nørskov, J. K. CatApp: A Web Application for Surface Chemistry and Heterogeneous Catalysis. *Angew. Chemie - Int. Ed.* **2012**, *51* (1), 272–274. https://doi.org/10.1002/anie.201107947.

(3) Engelmann, Y.; Mehta, P.; Neyts, E. C.; Schneider, W. F.; Bogaerts, A. Predicted

Influence of Plasma Activation on Nonoxidative Coupling of Methane on Transition Metal Catalysts. *ACS Sustain. Chem. Eng.* **2020**, *8* (15), 6043–6054. https://doi.org/10.1021/acssuschemeng.0c00906.

(4) Campbell, C. T.; Sprowl, L. H.; Árnadóttir, L. Equilibrium Constants and Rate Constants for Adsorbates: Two-Dimensional (2D) Ideal Gas, 2D Ideal Lattice Gas, and Ideal Hindered Translator Models. *J. Phys. Chem. C* **2016**, *120* (19), 10283–10297. https://doi.org/10.1021/acs.jpcc.6b00975.

(5) van ‘t Veer, K.; Engelmann, Y.; Reniers, F.; Bogaerts, A. Plasma-Catalytic Ammonia Synthesis in a DBD Plasma: Role of Microdischarges and Their Afterglows. *J. Phys. Chem. C* **2020**, *124* (42), 22871–22883. https://doi.org/10.1021/acs.jpcc.0c05110.

(6) Huygh, S.; Neyts, E. C. Adsorption of C and CHx Radicals on Anatase (001) and the Influence of Oxygen Vacancies. *J. Phys. Chem. C* **2015**, *119* (001), 4908–4921. https://doi.org/10.1021/jp5127249.

(7) Tada, K.; Maruyama, T.; Koga, H.; Okumura, M.; Tanaka, S. Extent of Spin Contamination Errors in DFT/Plane-Wave Calculation of Surfaces: A Case of Au Atom Aggregation on a MgO Surface. *Molecules* **2019**, *24* (3). https://doi.org/10.3390/molecules24030505.

(8) Rouwenhorst, K. H. R.; Lefferts, L. On the Mechanism for the Plasma-Activated N2 Dissociation on Ru Surfaces. *J. Phys. D. Appl. Phys.* **2021**, *54*, 393002. https://doi.org/https://doi.org/10.1088/1361-6463/ac1226.